

---

*This copy is for your personal, non-commercial use only.*

---

**If you wish to distribute this article to others**, you can order high-quality copies for your colleagues, clients, or customers by [clicking here](#).

**Permission to republish or repurpose articles or portions of articles** can be obtained by following the guidelines [here](#).

**The following resources related to this article are available online at [www.sciencemag.org](http://www.sciencemag.org) (this information is current as of April 15, 2014 ):**

**Updated information and services**, including high-resolution figures, can be found in the online version of this article at:

<http://www.sciencemag.org/content/290/5492/773.full.html>

A list of selected additional articles on the Science Web sites **related to this article** can be found at:

<http://www.sciencemag.org/content/290/5492/773.full.html#related>

This article **cites 24 articles**, 2 of which can be accessed free:

<http://www.sciencemag.org/content/290/5492/773.full.html#ref-list-1>

This article has been **cited by** 497 article(s) on the ISI Web of Science

This article has been **cited by** 12 articles hosted by HighWire Press; see:

<http://www.sciencemag.org/content/290/5492/773.full.html#related-urls>

This article appears in the following **subject collections**:

Physics

<http://www.sciencemag.org/cgi/collection/physics>

$\mu\text{g/ml}$  pepstatin, 4 mM PMSF, and 0.5% NP-40) was then added. The tubes were shaken for 2 hours in the The supernatant was collected for ELISA and protein measurements. The ELISA reaction was completed in 96-well plate (Dynatech, Chantilly, VA) according to the ELISA manufacturer's instructions (GDNF E<sub>max</sub> ImmunoAssay Systems Kit G3520, Promega, Madison, WI). The optical densities were recorded in ELISA plate reader (at 450 nm wave length; Dynatech). Some lysates were diluted to ensure all the optical densities were within the standard curve. The con-

centrations or GDNF were calculated against six-point standard curve and then adjusted to picograms of GDNF per milligram of total protein. The total protein in each tissue lysate was measured using Bio-Rad protein assay kit (Bio-Rad, Richmond, CA).

28. D. A. Kozłowski *et al.*, *ASNT*, Abstr. 7, 25 (2000).
29. J. L. Eberling *et al.*, *Brain Res.* **832**, 184 (1999).
30. B. Connor *et al.*, *Gene Ther.* **6**, 1936 (1999).
31. C. Rosenblad, D. Kirik, A. Björklund, *Exp. Neurol.* **16**, 503 (2000).
32. This research was supported by a grant from the

Department of Defense, The Charles Shapiro Foundation, NS40578, and by the Swiss National Science Foundation and the Swiss National Program in Neurological Diseases. We thank T. Collier for comments on this manuscript, T. Kladis and J. Stansell for expert histological assistance, F. Pidoux and M. Rey for the technical assistance in the production of the lentiviral vectors, K. Gibbons for assistance with PET scans, and J. Sladek Jr. for photographic assistance.

9 December 1999; accepted 17 August 2000

# Quantum Superposition of Macroscopic Persistent-Current States

Caspar H. van der Wal,<sup>1\*</sup> A. C. J. ter Haar,<sup>1</sup> F. K. Wilhelm,<sup>1</sup>  
R. N. Schouten,<sup>1</sup> C. J. P. M. Harmans,<sup>1</sup> T. P. Orlando,<sup>2</sup>  
Seth Lloyd,<sup>3</sup> J. E. Mooij<sup>1,2</sup>

Microwave spectroscopy experiments have been performed on two quantum levels of a macroscopic superconducting loop with three Josephson junctions. Level repulsion of the ground state and first excited state is found where two classical persistent-current states with opposite polarity are degenerate, indicating symmetric and antisymmetric quantum superpositions of macroscopic states. The two classical states have persistent currents of 0.5 microampere and correspond to the center-of-mass motion of millions of Cooper pairs.

When a small magnetic field is applied to a superconducting loop, a persistent current is induced. Such a persistent supercurrent also occurs when the loop contains Josephson tunnel junctions. The current is clockwise or counterclockwise, thereby either reducing or enhancing the applied flux to approach an integer number of superconducting flux quanta  $\Phi_0$  (*1*). In particular when the enclosed magnetic flux is close to half-integer values of  $\Phi_0$ , the loop may have multiple stable persistent-current states, with at least two of opposite polarity. The weak coupling of the Josephson junctions then allows for transitions between the states. Previous theoretical work (*2–4*) proposed that a persistent current in a loop with Josephson junctions corresponds to the center-of-mass motion of all the Cooper pairs in the system and that quantum mechanical behavior of such persistent-current states would be a manifestation of quantum mechanical behavior of a macroscopic object. In a micrometer-sized loop, millions of Cooper pairs are involved. At very low temperatures, excitations of individual charge carriers around the center of mass

of the Cooper-pair condensate are prohibited by the superconducting gap. As a result, the coupling between the dynamics of persistent supercurrents and many-body quasi-particle states is very weak. Josephson junction loops therefore rank among the best objects for experimental tests of the validity of quantum mechanics for systems containing a macroscopic number of particles (*3, 5, 6*) [loss of quantum coherence results from coupling to an environment with many degrees of freedom (*7*)] and for research on the border between classical and quantum physics. The potential for quantum coherent dynamics has stimulated research aimed at applying Josephson junction loops as basic building blocks for quantum computation (qubits) (*8–11*).

We present microwave spectroscopy experiments that demonstrate quantum superpositions of two macroscopic persistent-current states in a small loop with three Josephson junctions (Fig. 1A). At an applied magnetic flux of  $\frac{1}{2}\Phi_0$ , the system behaves as a particle in a double-well potential, where the classical states in each well correspond to persistent currents of opposite sign. The two classical states are coupled via quantum tunneling through the barrier between the wells, and the loop is a macroscopic quantum two-level system (Fig. 1B) (*12*). The energy levels vary with the applied flux as shown (Fig. 1C). Classically, the levels cross at  $\frac{1}{2}\Phi_0$ . Tunneling between the wells leads to quantum mechanical eigenstates that at  $\frac{1}{2}\Phi_0$  are symmet-

ric and antisymmetric superpositions of the two classical persistent-current states. The symmetric superposition state is the quantum mechanical ground state with an energy lower than the classical states; the antisymmetric superposition state is the loop's first excited state with an energy higher than the classical states. Thus, the superposition states manifest themselves as an anticrossing of the loop's energy levels near  $\frac{1}{2}\Phi_0$ . We performed spectroscopy on the loop's two quantum levels (Fig. 2) and our results show the expected anticrossing at  $\frac{1}{2}\Phi_0$  (Fig. 3) (*13*). We also studied the resonance-line shapes and found behavior similar to microscopic quantum two-level systems (*14, 15*) (Fig. 4).

**Detecting quantum superposition.** In our experiments, the magnetic flux generated by the loop's persistent current was measured with an inductively coupled direct-current superconducting quantum interference device (DC-SQUID) (Figs. 1 and 2), while low-amplitude microwaves were applied to induce transitions between the levels. We observed narrow resonance lines at magnetic field values where the level separation  $\Delta E$  was resonant with the microwave frequency. The DC-SQUID performs a measurement on a single quantum system. Thus, we should expect that the measurement process limits the coherence of our system. While the system is pumped by the microwaves, the SQUID actively measures the flux produced by the persistent currents of the two states. Detecting the quantum levels of the loop is still possible because the meter is only weakly coupled to the loop. The flux signal needs to be built up by averaging over many repeated measurements on the same system (Fig. 2B), such that an ensemble average is effectively determined. We measure the level separation, i.e., energy rather than flux, as we perform spectroscopy, and we observe a change in averaged flux when the microwaves are resonant with the level separation (the peaks and dips in Figs. 2B and 3A). We also chose to work with an extremely underdamped DC-SQUID with unshunted junctions to minimize damping of the quantum system via the inductive coupling to the SQUID.

Similar observations were recently made by Friedman *et al.* (*16*) who performed spectroscopy on excited states in a loop with a

<sup>1</sup>Department of Applied Physics and Delft Institute for Micro Electronics and Submicron Technology (DIMES), Delft University of Technology, Post Office Box 5046, 2600 GA Delft, Netherlands. <sup>2</sup>Department of Electrical Engineering and Computer Science and <sup>3</sup>Department of Mechanical Engineering, Massachusetts Institute of Technology, Cambridge, MA 02139, USA.

\*To whom correspondence should be addressed. E-mail: caspar@qt.tn.tudelft.nl

single Josephson junction (radio frequency SQUID). Previous experiments with single-junction loops have demonstrated resonant tunneling between discrete quantum states in two wells (17, 18) and microwave-induced transitions between the wells (19, 20). Other observations related to macroscopic superposition states are tunnel splittings observed with magnetic molecular clusters (21, 22) and quantum interference of  $C_{60}$  molecules (23). In quantum dots (24) and superconducting circuits where charge effects dominate over the Josephson effect (25–27), superpositions of charge states have been observed, as well as quantum coherent charge oscillations (28).

**Macroscopic quantum system.** Our quantum system is a low-inductance loop intersected by three Josephson tunnel junctions (Fig. 1A) (10, 11). The Josephson junctions are extremely underdamped and are characterized by their Josephson coupling  $E_J$  and charging energy  $E_C = e^2/2C$ , where  $C$  is the junction capacitance and  $e$  is the electron charge. The critical current of a junction is  $I_{C0} = \frac{2e}{\hbar} E_J$ , where  $\hbar = \frac{h}{2\pi}$  is the reduced Planck constant. One of the junctions in the loop has  $E_J$  and  $C$  smaller by a factor  $\beta \approx 0.8$ . At an applied flux  $\Phi_{\text{ext}}$  close to  $\frac{1}{2}\Phi_0$ , the total Josephson energy forms a double-well potential. The classical states at the bottom of

each well have persistent currents of opposite sign, with a magnitude  $I_p$  very close to  $I_{C0}$  of the weakest junction and with energies  $E = \pm I_p(\Phi_{\text{ext}} - \frac{1}{2}\Phi_0)$  (dashed lines in Fig. 1C) (29). The system can be pictured as a particle with a mass proportional to  $C$  in the Josephson potential; the electrostatic energy is the particle's kinetic energy. The charging effects are conjugate to the Josephson effect. For low-capacitance junctions (small mass) quantum tunneling of the particle through the barrier gives a tunnel coupling  $t$  between the persistent-current states. In the presence of quantum tunneling and for  $E_J/E_C$  values between 10 and 100, the system should have two low-energy quantum levels  $E_0$  and  $E_1$ , which can be described using a simple quantum two-level picture (10, 11),

$$E_{0(1)} = -(+) \sqrt{t^2 + [I_p(\Phi_{\text{ext}} - \frac{1}{2}\Phi_0)]^2}$$

The loop's level separation  $\Delta E = E_1 - E_0$  is then

$$\Delta E = \sqrt{(2t)^2 + [2I_p(\Phi_{\text{ext}} - \frac{1}{2}\Phi_0)]^2} \quad (1)$$

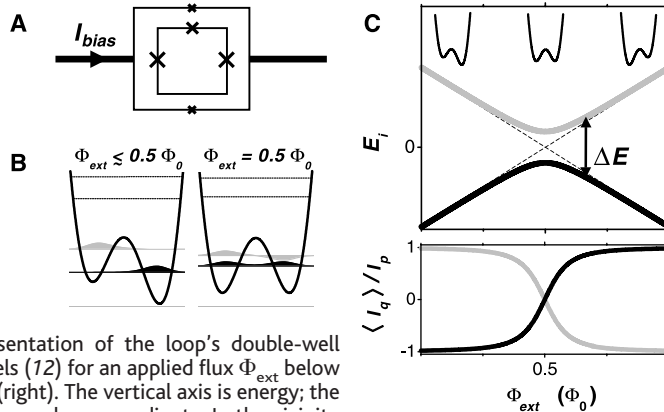
The system was realized by microfabricating an aluminum micrometer-sized loop with unshunted Josephson junctions (30). Around the loop, we fabricated the DC-SQUID magnetometer (Fig. 1A), which contains smaller Josephson junctions that were as under-

damped as the junctions of the inner loop. Loop parameters estimated from test junctions fabricated on the same chip and electron microscope inspection of the measured device give  $I_{C0} = 570 \pm 60$  nA and  $C = 2.6 \pm 0.4$  fF for the largest junctions in the loop and  $\beta = 0.82 \pm 0.1$ , giving  $E_J/E_C = 38 \pm 8$  and  $I_p = 450 \pm 50$  nA. Due to the exponential dependence of the tunnel coupling  $t$  on the mass (i.e., the capacitance  $C$ ) and the size of the tunnel barrier, these parameters allow for a value for  $t/h$  between 0.2 and 5 GHz. The parameters of the DC-SQUID junctions were  $I_{C0} = 109 \pm 5$  nA and  $C = 0.6 \pm 0.1$  fF. The self inductance of the inner loop and the DC-SQUID loop were estimated to be  $11 \pm 1$  picoHenry (pH) and  $16 \pm 1$  pH, respectively, and the mutual inductance  $M$  between the loop and the SQUID was  $7 \pm 1$  pH (31). The flux in the DC-SQUID is measured by ramping a bias current through the DC-SQUID and recording the current level  $I_{\text{SW}}$  where the SQUID switches from the supercurrent branch to a finite voltage (Fig. 2A). Traces of the loop's flux signal were recorded by continuously repeating switching-current measurements while slowly sweeping the flux  $\Phi_{\text{ext}}$  (Fig. 2B). The measured flux signal from the inner loop will be presented as  $\bar{I}_{\text{SW}}$ , which is an averaged value directly deduced from the raw switching-current data (32).

**Results.** Figure 3A shows the flux signal of the inner loop, measured in the presence of low-amplitude continuous-wave microwaves at different frequencies  $f$ . The rounded step in each trace at  $\frac{1}{2}\Phi_0$  is due to the change in direction of the persistent current of the loop's ground state (see also Fig. 1C). Symmetrically around  $\Phi_{\text{ext}} = \frac{1}{2}\Phi_0$  each trace shows a peak and a dip, which were absent when no microwaves were applied. The positions of the peaks and dips in  $\Phi_{\text{ext}}$  depend on microwave frequency but not on amplitude. The peaks and dips result from microwave-induced transitions to the state with a persistent current of opposite sign. These occur when the level separation is resonant with the microwave frequency,  $\Delta E = hf$ .

In Fig. 3B, half the distance in  $\Phi_{\text{ext}}$  between the resonant peak and dip  $\Delta\Phi_{\text{res}}$  is plotted for all the frequencies  $f$ . The relation between  $\Delta E$  and  $\Phi_{\text{ext}}$  is linear for the high-frequency data. This gives  $I_p = 484 \pm 2$  nA, in good agreement with the predicted value. At lower frequencies,  $\Delta\Phi_{\text{res}}$  significantly deviates from this linear relation, demonstrating the presence of a finite tunnel splitting at  $\Phi_{\text{ext}} = \frac{1}{2}\Phi_0$ . A fit to Eq. 1 yields  $t/h = 0.33 \pm 0.03$  GHz, in agreement with the estimate from fabrication parameters. The level separation very close to  $\frac{1}{2}\Phi_0$  could not be measured directly because at this point the expectation value for the persistent current is zero for both the ground state and the excited state (Fig. 1C). Nevertheless, the narrow res-

**Fig. 1.** (A) Schematic of the small superconducting loop with three Josephson junctions (denoted by the crosses). The loop is inductively coupled to an underdamped DC-SQUID, which is positioned around the loop. The DC-SQUID can be used as a magnetometer by applying a bias current  $I_{\text{bias}}$  to it. (B) Schematic presentation of the loop's double-well potential with energy levels (12) for an applied flux  $\Phi_{\text{ext}}$  below  $\frac{1}{2}\Phi_0$  (left) and at  $\frac{1}{2}\Phi_0$  (right). The vertical axis is energy; the horizontal axis is a Josephson phase coordinate. In the vicinity of  $\Phi_{\text{ext}} = \frac{1}{2}\Phi_0$ , the loop is a double-well system in which the two minima correspond to classical states with persistent currents of equal magnitude  $I_p$ , but with opposite polarity. Quantum mechanically, the system has two low-energy eigen states (black and gray) that are well separated in energy from higher excited states (dashed lines), such that it is effectively a quantum two-level system. The shape of the wave function of the ground state (black) and first excited state (gray) is shown at the energy level. For  $\Phi_{\text{ext}}$  below or above  $\frac{1}{2}\Phi_0$  the two lowest eigen states are well localized on either side of the barrier and correspond (apart from zero-point energy) to the classical persistent-current states. When quantum tunneling between the wells is possible, the loop's eigen states are at  $\Phi_{\text{ext}} = \frac{1}{2}\Phi_0$ , symmetric and antisymmetric superpositions of the two persistent-current states. The schematic plots show a distribution of the levels in the potential that is typical for the device parameters mentioned in the text. (C) Energy levels and persistent currents of the loop as a function of applied flux  $\Phi_{\text{ext}}$ . The insets of the top plot show again the double-well potential, for  $\Phi_{\text{ext}}$  below  $\frac{1}{2}\Phi_0$  (left), at  $\frac{1}{2}\Phi_0$  (middle), and above  $\frac{1}{2}\Phi_0$  (right). The energies of the two localized persistent-current states are indicated with the dashed lines, and they cross at  $\Phi_{\text{ext}} = \frac{1}{2}\Phi_0$ . The quantum levels (solid lines) show an anti-crossing near  $\Phi_{\text{ext}} = \frac{1}{2}\Phi_0$  where the eigen states are symmetric and antisymmetric superpositions of the two persistent-current states. The level of the ground state  $E_0$  (black) and the excited state  $E_1$  (gray) are separated in energy by  $\Delta E$ . The bottom plot shows the quantum mechanical expectation value  $\langle I_p \rangle = -\partial E_i / \partial \Phi_{\text{ext}}$  of the persistent current in the loop, for the ground state  $E_0$  (black) and the excited state  $E_1$  (gray), plotted in units of the classical magnitude of the persistent currents  $I_p$ .



onance lines allow for an accurate mapping of the level separation near  $\frac{1}{2}\Phi_0$ , and the observed tunnel splitting gives clear evidence for quantum superpositions of the persistent-current states. The large uncertainty in the predicted  $t$  value does not allow for a quantitative analysis of a possible suppression of  $t$  due to a coupling between our two-level system and a bosonic environment (33) or a spin-bath environment (34, 35). However, the fact that we see a finite tunnel splitting indicates that the damping of our quantum system, which is caused by environmental degrees of freedom, is weak. The dimensionless dissipation parameter  $\alpha$  introduced by Leggett *et al.* (33) must be  $\alpha < 1$ .

In Fig. 4, we show the dependence of the dip shape at 5.895 GHz on applied microwave amplitude. The dip amplitude and the full width at half the maximum amplitude (FWHM) were estimated for different microwave amplitudes by fitting a Lorentzian peak shape to the data. Figure 4B shows that the dip amplitude increases rapidly for microwave amplitudes up to  $V_{AC} \approx 2$  arbitrary units (a.u.), followed by a saturation for larger microwave amplitudes. The saturated dip amplitude is  $\approx 0.25$  nA, which is close to half the full step height of the rounded step at  $\frac{1}{2}\Phi_0$  ( $\approx 0.4$  nA) in Fig. 3A. This indicates that on resonance the energy levels are close to being equally populated, as expected for pumping with continuous-wave microwaves.

Figure 4C shows a linear dependence between the FWHM and the microwave amplitude. Qualitatively, this dependence of the line shape on microwave amplitude agrees with spectroscopy results on microscopic quantum two-level systems. For negligible decoherence, spectroscopy on quantum two-level systems yields a Lorentzian line shape and transitions between the levels occur by coherent Rabi oscillations. The FWHM of the Lorentzian resonance line is two times the Rabi frequency and is proportional to the amplitude of the monochromatic perturbation (14). The linear dependence of the FWHM on microwave amplitude in Fig. 4C suggests that the line width for  $V_{AC} > 2$  a.u. is dominated by the frequency of microwave-induced Rabi transitions. Transitions occur then by a few quantum coherent Rabi cycles. Using the linear relation between  $\Delta E$  and  $\Phi_{ext}$  for  $\Phi_{ext}$  values away from  $\frac{1}{2}\Phi_0$ , the observed FWHM in  $\Phi_{ext}$  units can be expressed in frequency units. This indicates a Rabi frequency of, for example, 150 MHz at  $V_{AC} = 4$  a.u. However, we do not consider these results as proof for coherent quantum dynamics because other scenarios with weak decoherence give similar results (36).

#### Dephasing due to measuring SQUID.

The loss of dip amplitude and the apparent saturation of the FWHM at low  $V_{AC}$  is caused either by variations in the flux bias  $\Phi_{ext}$

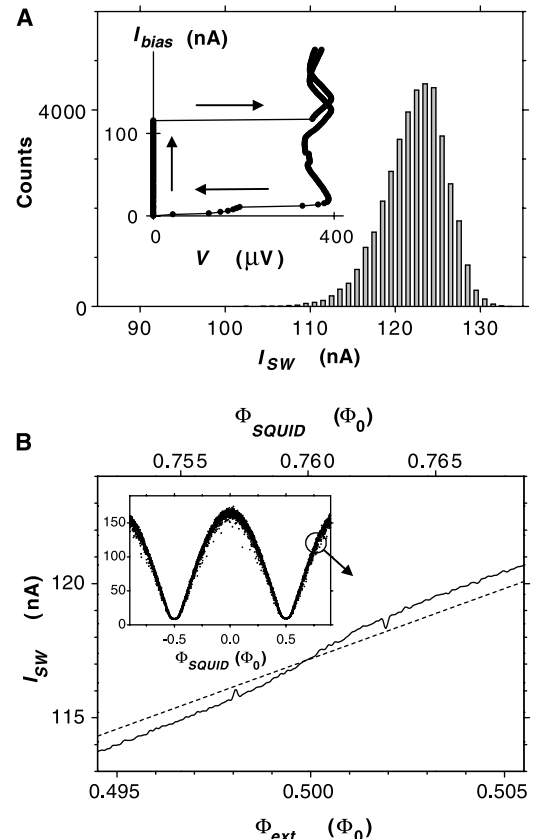
[corresponding to inhomogeneous broadening for the ensemble average (15)] or by an intrinsic dephasing mechanism. The effective dephasing time  $T_2^*$  (15) can be deduced from the FWHM at low  $V_{AC}$ . The FWHM (expressed in energy units) of a resonance line shape that is dominated by a finite dephasing time corresponds to  $\frac{2h}{T_2^*}$  (15, 14). Using, once more, the linear relation between  $\Delta E$  and  $\Phi_{ext}$  for  $\Phi_{ext}$  values away from  $\frac{1}{2}\Phi_0$  to express the FWHM at  $V_{AC} = \approx 2$  a.u. in energy units, gives  $T_2^* \approx 15$  ns. As discussed below, this can be fully explained by variations in the applied magnetic flux that originate from the measuring DC-SQUID.

The DC-SQUID performs a weak measurement on the loop. It has two macroscopic phase degrees of freedom. One is associated with the circulating current in the SQUID's loop (internal degree of freedom), the other is associated with the bias current through the SQUID (external degree of freedom). As the bias current is ramped up, the coupling between these two degrees of freedom increases strongly due to the nonlinearity of the SQUID's current-phase relations ( $I$ ). The external variable is coupled to a dissipative environment, and the associated effective mass (i.e., the capacitance across the SQUID) is very large. The internal degree of freedom

has negligible intrinsic damping and the associated mass (i.e., the capacitance of the junctions of the SQUID) is very small. Consequently, this variable exhibits quantum behavior. The classical external degree of freedom of the SQUID performs a measurement on the SQUID's inner quantum variable, which in turn is weakly coupled to our quantum loop. We therefore expect that the SQUID contributes dominantly to the loop's dephasing and damping with the present setup. The choice for an underdamped DC-SQUID resulted in very wide switching-current histograms. The width of the histogram corresponds to a standard deviation in the flux readout of  $11 \cdot 10^{-3} \Phi_0$ . The uncertainty in flux readout is much larger than the flux signal from the inner loop  $2M I_p \approx 3 \cdot 10^{-3} \Phi_0$ . Therefore, we can only detect the loop's signal by averaging over many switching events (Fig. 2).

The loss of dip amplitude in Fig. 4 is probably due to a small contribution to the effective  $\Phi_{ext}$  from the circulating current in the DC-SQUID. The SQUID is operated at  $0.76 \Phi_0$  in its loop, where its circulating current depends on the bias current due to its nonlinear behavior ( $I$ ). This means that data recorded by switching events on the low  $I_{bias}$  side of the FWHM of the  $I_{sw}$  histogram in Fig. 2A differs in flux bias on the inner loop from that of the high side by  $20 \cdot 10^{-6} \Phi_0$ .

**Fig. 2. (A)** Current-voltage characteristic (inset) and switching-current histogram of the underdamped DC-SQUID. The plot with bias current  $I_{bias}$  versus voltage  $V$  is strongly hysteretic. The  $I_{bias}$  level where the SQUID switches from the supercurrent branch to a finite voltage state—the switching current  $I_{sw}$ —is a measure for the flux in the loop of the DC-SQUID. Switching to the voltage state is a stochastic process. The histogram in the main plot shows that the variance in  $I_{sw}$  is much larger than the flux signal of the inner loop's persistent current, which gives a shift in the averaged  $I_{sw}$  of about 1 nA (see Fig. 2B). **(B)** Switching-current levels of the DC-SQUID versus applied flux. The inset shows the modulation of  $I_{sw}$  versus the flux  $\Phi_{SQUID}$  applied to the DC-SQUID loop (data not averaged, one point per switching event). The main figure shows the averaged level of  $I_{sw}$  (solid line) near  $\Phi_{SQUID} = 0.76 \Phi_0$ . At this point, the flux in the inner loop  $\Phi_{ext} \approx \frac{1}{2}\Phi_0$ . The rounded step at  $\Phi_{ext} = \frac{1}{2}\Phi_0$  indicates the change of sign in the persistent current of the loop's ground state. Symmetrically around  $\frac{1}{2}\Phi_0$  the signal shows a peak and a dip, which are only observed with measurements in the presence of continuous-wave microwaves (here 5.895 GHz). The peak and dip are due to resonant transitions between the loop's two quantum levels (Fig. 3). The background signal of the DC-SQUID that results from flux directly applied to its loop (dashed line) is subtracted from the data presented in Figs. 3A and 4A.





Resonance lines at low  $V_{AC}$  (i.e., with a  $\text{FWHM} < 20 \cdot 10^{-6} \Phi_0$ ) cannot be observed as the peaks and dips smear out when averaging over many switching events. The loss of dip amplitude and the apparent saturation of the FWHM at low  $V_{AC}$  is probably dominated by this mechanism for inhomogeneous line broadening.

The width of the rounded steps in the measured flux in Fig. 3A is much broader

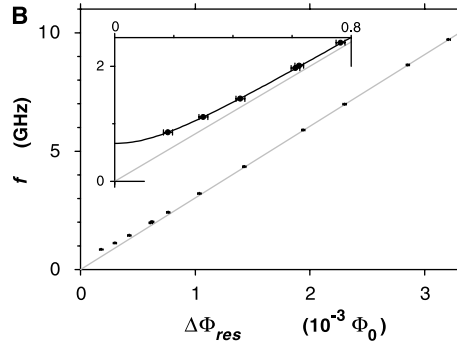
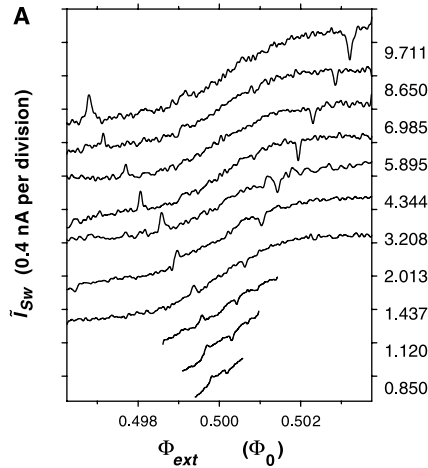
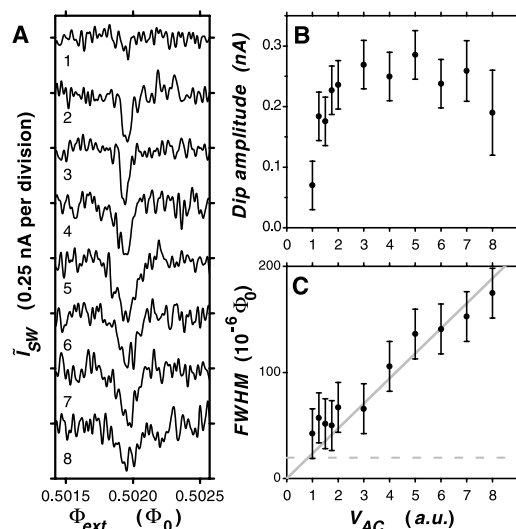


**Fig. 3.** (A) Switching-current levels  $\bar{I}_{SW}$  of the DC-SQUID as a function of  $\Phi_{ext}$ , measured at different microwave frequencies  $f$  [labels on the right give  $f$  in GHz,  $\bar{I}_{SW}$  is deduced from the raw switching-current data  $I_{SW}$  by averaging and subtracting a background signal (32)]. Each trace clearly shows the rounded step at  $\Phi_{ext} = 1/2\Phi_0$  where the persistent current of the loop's ground state changes sign. In the presence of continuous-wave microwaves a peak and a dip appear in the signal, symmetrically around  $1/2\Phi_0$ . The positions of the peak and dip depend on  $f$ . The peak and dip appear at values of  $\Phi_{ext}$  where the level separation between the lowest quantum states of the loop is resonant with the microwave frequency, and the microwaves induce transitions to the state that has a persistent current of opposite sign. (B) Half the distance in  $\Phi_{ext}$  between the resonant peak and dip  $\Delta\Phi_{res}$  at different microwave frequencies  $f$  ( $f$  is plotted on the vertical axis for compatibility with Fig. 1C). Peak and dip positions are determined from traces as in (A). At high frequencies, the  $\Delta\Phi_{res}$  values are proportional to the microwave frequency. The gray line is a linear fit through the high-frequency data points and zero. The slope is used to determine  $I_p = 484$  nA. At low microwave frequencies the measured  $\Delta\Phi_{res}$  values deviate significantly from this linear relation, demonstrating that the loop's lowest two energy levels repel each other near  $\Phi_{ext} = 1/2\Phi_0$ . The inset zooms in on the low-frequency data points. The black line is a fit of Eq. 1 with only the tunnel coupling  $t$  as a fitting parameter, yielding  $t/h = 0.33 \pm 0.03$  GHz.

**Fig. 4.** (A) The influence of the microwave amplitude on the shape of the resonance dip in the scaled switching current  $\bar{I}_{SW}$ , measured at 5.895 GHz [the labels on the left give the amplitude  $V_{AC}$  in a.u.]. (B) The dip amplitude first increases with microwave amplitude  $V_{AC}$ , but saturates at  $V_{AC} > 2$  a.u. (C) The FWHM of the dips increases with  $V_{AC}$ . The linear fit through the highest data points and zero (gray) is a guide to the eye. The horizontal dashed line indicates a flux value that corresponds to the shift in effective flux bias  $\Phi_{ext}$  which is induced when the bias current is ramped through the DC-SQUID. This acts as a flux instability with an amplitude of  $\approx 20 \cdot 10^{-6} \Phi_0$ . Resonance lines with a FWHM below this value cannot be observed. The loss of dip amplitude in Fig. 4B when lowering  $V_{AC} < 2$  a.u. sets in where the  $\text{FWHM} \approx 20 \cdot 10^{-6} \Phi_0$ . The flux shift from the SQUID is calculated using the  $I_{bias}$  interval (the FWHM of the switching-current histogram is used) where the SQUID typically switches.



( $k_B$  is Boltzmann's constant), where we use the level separation  $\Delta E$  and  $I_p$  found with spectroscopy. However, at low temperatures the observed step width saturates at an effective temperature of about 100 mK. We checked that the effective temperature for the SQUID's switching events did not saturate at the lowest temperatures. The high effective temperature of the loop is a result of the loop being in a nonequilibrium state. The population of the excited state could be caused by the measuring SQUID or other weakly coupled external processes.

**Concluding remarks and future prospects.** The data presented here provide clear evidence that a small Josephson junction loop can behave as a macroscopic quantum two-level system. The application of an underdamped DC-SQUID for measuring the loop's magnetization is a useful tool for future work on quantum coherent experiments with Josephson junction loops. The present results also demonstrate the potential of three-junction persistent-current loops for research on macroscopic quantum coherence and for use as qubits in a quantum computer. This requires quantum-state control with pulsed microwaves and development of measurement schemes that are less invasive. Circuits that contain multiple qubits with controlled inductive coupling are within reach using present-day technology.

## References and Notes

1. M. Tinkham, *Introduction to Superconductivity* (McGraw-Hill, New York, ed. 2, 1996), pp. 196–234.
2. P. W. Anderson, in *Lectures on the Many-Body Problem*, E. R. Caianiello, Ed. (Academic Press, New York, 1964), vol. 2, pp. 113–135.
3. A. J. Leggett, *Prog. Theor. Phys. Suppl.* **69**, 80 (1980).
4. K. K. Likharev, *Sov. Phys. Usp.* **26**, 87 (1983).
5. A. J. Leggett, A. Garg, *Phys. Rev. Lett.* **54**, 857 (1985).
6. A. J. Leggett, *J. Supercond.* **12**, 683 (1999).
7. W. H. Zurek, *Phys. Today* **44**, 36 (October 1991).
8. M. F. Bocko, A. M. Herr, M. J. Feldman, *IEEE Trans. Appl. Supercond.* **7**, 3638 (1997).
9. L. B. Ioffe, V. B. Geshkenbein, M. V. Feigel'man, A. L. Fauchère, G. Blatter, *Nature* **398**, 679 (1999).
10. J. E. Mooij *et al.*, *Science* **285**, 1036 (1999).
11. T. P. Orlando *et al.*, *Phys. Rev. B* **60**, 15398 (1999).
12. The double-well potential shown in Fig. 1B is the relevant potential for the tunnel transitions between the system's two persistent-current states. The potential is the sum of the Josephson energies of all the junctions and the zero-point energy of a Josephson phase degree of freedom that is perpendicular to the tunnel direction between the two wells (10, 11). This zero-point energy is nearly constant along the tunnel trajectory between the wells, and it has a plasma frequency much higher than the level separation between the lowest two quantum levels. It should therefore be included in the effective potential for transitions between the two wells. For the sample parameters mentioned in the text the lowest two quantum levels are well below the top of the effective tunnel barrier.
13. The results presented here do not exclude alternative theories for quantum mechanics [e.g., macro-realistic theories (37)]. This would require a type of experiment as proposed by Leggett *et al.* (5).
14. C. Cohen-Tannoudji, B. Diu, F. Laloë, *Quantum Mechanics* (Wiley, New York, 1977), vol. 1, pp. 443–454.
15. A. Abragam, *Principles of Nuclear Magnetism* (Oxford Univ. Press, Oxford, 1961), pp. 39–57.
16. J. R. Friedman, V. Patel, W. Chen, S. K. Tolpygo, J. E. Lukens, *Nature* **406**, 43 (2000).

17. R. Rouse, S. Han, J. E. Lukens, *Phys. Rev. Lett.* **75**, 1614 (1995).
18. C. Cosmelli et al., *Phys. Rev. Lett.* **82**, 5357 (1999).
19. S. Han, R. Rouse, J. E. Lukens, *Phys. Rev. Lett.* **76**, 3404 (1996).
20. ———, *Phys. Rev. Lett.* **84**, 1300 (2000).
21. W. Wernsdorfer, R. Sessoli, *Science* **284**, 133 (1999).
22. E. del Barco et al., *Europhys. Lett.* **47**, 722 (1999).
23. M. Arndt et al., *Nature* **401**, 680 (1999).
24. T. H. Oosterkamp et al., *Nature* **395**, 873 (1998).
25. Y. Nakamura, C. D. Chen, J. S. Tsai, *Phys. Rev. Lett.* **79**, 2328 (1997).
26. V. Bouchiat, D. Vion, P. Joyez, D. Esteve, M. H. Devoret, *Phys. Scr.* **176**, 165 (1998).
27. D. J. Flees, S. Han, J. E. Lukens, *J. Supercond.* **12**, 813 (1999).
28. Y. Nakamura, Yu. A. Pashkin, J. S. Tsai, *Nature* **398**, 786 (1999).
29. The small self-generated flux due to the persistent currents leads to a constant lowering of the energies. The crossing remains at  $1/2\Phi_0$ . In the discussion we take  $\Phi_{\text{ext}}$  to be the total flux in the loop.
30. The sample consisted of a 5  $\mu\text{m}$  by 5  $\mu\text{m}$  aluminum loop with aluminum oxide tunnel junctions, micro-fabricated with e-beam lithography and shadow-evaporation techniques on a  $\text{SiO}_2$  substrate. The lines of the loop were 450-nm wide and 80-nm thick. A DC-SQUID with a 7  $\mu\text{m}$  by 7  $\mu\text{m}$  loop was fabricated in the same layer around the inner loop. The DC-SQUID had an on-chip superconducting shunt capacitance of 2 pF and superconducting leads in a four-point configuration. The sample was mounted in a dilution refrigerator, inside a microwave-tight copper measurement box, magnetically shielded by two

high-permeability metal shields and one superconducting shield. All spectroscopy measurements were taken with the temperature stabilized at  $30 \pm 0.05$  mK. Microwaves were applied to the sample by a coaxial line, which was shorted at the end by a small loop of 5-mm diameter. This loop was positioned parallel to the sample plane at about 1 mm distance. Switching currents were measured with dedicated electronics, with repetition rates up to 9 kHz and bias currents ramped at typically 1  $\mu\text{A/ms}$ . A detailed description of the fabrication and experimental techniques can be found in [C. H. van der Wal, J. E. Mooij, *J. Supercond.* **12**, 807 (1999)].

31. The inductances were estimated numerically from the geometry with a finite-element method. The value for  $M$  is in agreement with the flux signal from the inner loop (estimated from the step height in flux units in Fig. 2B) divided by  $\Phi_0$ .
32. Deducing  $I_{\text{SW}}$  from the raw switching-current data  $I_{\text{SW}}$  concerned the following three points: (i) Because the variance in  $I_{\text{SW}}$  was much larger than the signature from the loop's flux (Fig. 2), we applied low-pass FFT-filtering in  $\Phi_{\text{ext}}$  space (over  $10^7$  switching events for the highest trace, and  $2 \cdot 10^8$  events for the lowest trace in Fig. 3A). We checked that the cutoff frequency was chosen high enough not to influence any parameters deduced from the data. (ii) By applying  $\Phi_{\text{ext}}$ , we also apply flux directly to the DC-SQUID. The resulting background signal was subtracted (Fig. 2B). We checked that the estimated dip and peak positions in Fig. 3B did not depend significantly on subtracting a background signal. (iii) Applying microwaves and changing the sample temperature influenced the switching-current levels substantially. To

make the flux signal of all data sets comparable, we scaled all data sets to  $I_{\text{SW}} = 100$  nA at  $\Phi_{\text{ext}} = 1/2\Phi_0$ . Any uncertainty coming from this scaling is accounted for in the error bars in Figs. 3 and 4. Data taken in the presence of microwaves could only be obtained at specific frequencies where  $I_{\text{SW}}$  was not strongly suppressed by the microwaves. At temperatures above 300 mK, drift in the  $I_{\text{SW}}$  level due to thermal instabilities of the refrigerator obscured the signal.

33. A. J. Leggett et al., *Rev. Mod. Phys.* **59**, 1 (1987).
34. N. Prokof'ev, P. Stamp, *Rep. Prog. Phys.* **63**, 669 (2000) (e-Print available at <http://xxx.lanl.gov/abs/cond-mat/0001080>).
35. L. Tian et al., in *Quantum Mesoscopic Phenomena and Mesoscopic Devices in Microelectronics, Proceedings of a NATO-ASI Workshop*, in press (e-Print available at <http://xxx.lanl.gov/abs/cond-mat/9910062>).
36. M. Grifoni, P. Hänggi, *Phys. Rep.* **304**, 229 (1998).
37. For an in-depth discussion on macro-realism, see the essays of A. J. Leggett and A. Shimony in *Quantum Measurement: Beyond Paradox*, R. A. Healey, G. Hellman, Eds. (Univ. of Minnesota Press, Minneapolis, 1998), pp. 1–31.
38. We thank J. B. Majer, A. C. Wallast, L. Tian, D. S. Crankshaw, J. Schmidt, A. Wallraff, L. Levitov, and D. Esteve for help and for stimulating discussions. This work was financially supported by the Dutch Foundation for Fundamental Research on Matter (FOM), the European TMR research network on superconducting nanocircuits (SUPNAN), the U.S. Army Research Office (grant DAAG55-98-1-0369), and the NEDO joint research program (NTDP-98).

11 July 2000; accepted 8 September 2000

## REPORTS

## Triple Vortex Ring Structure in Superfluid Helium II

Demosthenes Kivotides, Carlo F. Barenghi,\* David C. Samuels

Superfluids such as helium II consist of two interpenetrating fluids: the normal fluid and the superfluid. The helium II vortex ring has generally been considered merely as a superfluid object, neglecting any associated motion of the normal fluid. We report a three-dimensional calculation of the coupled motion of the normal-fluid and superfluid components, which shows that the helium II vortex ring consists of a superfluid vortex ring accompanied by two coaxial normal-fluid vortex rings of opposite polarity. The three vortex rings form a coherent, dissipative structure.

Vortex rings (1) have long been studied as ideal examples of organized flow structures. A large body of literature has been concerned with vortex rings in a zero-viscosity (inviscid) fluid in which the vortex core thickness is much smaller than the ring's radius. This mathematical idealization is realized in a quantum fluid (2, 3), helium II, which is a superposition of two fluid components: the normal fluid (which is a fluid with nonzero viscosity) and the superfluid (an inviscid fluid). The concept of the superfluid vortex ring (4) or loop has contributed to many advances

in superfluidity, ranging from vortex creation (5, 6) to turbulence (7–10). An example of this is the fundamental issue of quantum mechanical phase coherence and the onset of dissipation. Ions injected into superfluid helium II move without friction, provided that the speed does not exceed a critical value (11) above which superfluid vortex rings are created (5). Vortex creation (12, 13) and motion (14, 15) have been studied theoretically using various models and are also being investigated by atomic physicists in the context of Bose-Einstein condensation in clouds of alkaline atoms (15, 16). The concept of the vortex ring has been applied to interpretations of the nature of the roton (17–19) and the superfluid transition itself (20). Finally, vortex rings are important in the study of super-

fluid turbulence, which manifests itself as a disordered tangle of superfluid vortex loops (distorted vortex rings). Superfluid vortex lines may also end at walls, or at free surfaces, without forming closed loops. For simplicity, we will consider here a circular superfluid vortex ring, but our results should also apply to all superfluid vortex lines.

Recent experiments, such as the observation of decay rates of superfluid vorticity (21, 22) consistent with the decay rates of Navier-Stokes turbulence, motivate our study of the dynamical coupling between the superfluid vorticity and the normal-fluid component. Superfluid vorticity scatters (23) the thermal excitations that make up the normal fluid, producing a mutual friction acting on the velocity fields  $\mathbf{V}_s$  and  $\mathbf{V}_n$  of the two fluid components of helium II. Although the superfluid vorticity can be detected directly by the second sound technique (21), very little is actually known about the normal-fluid flow because we have no practical flow visualization techniques near absolute zero. We present results of a three-dimensional calculation in which  $\mathbf{V}_n$  and  $\mathbf{V}_s$  are determined self-consistently. The calculation reveals the surprising triple structure of the helium II vortex ring. We also discuss the implications of this finding for the interpretation of current turbulence experiments.

Our method is based on an improvement over the vortex dynamics approach of Schwarz (24, 25), who modeled a superfluid vortex line as a curve  $\mathbf{S}(\xi, t)$  that obeys the

Mathematics Department, University of Newcastle, Newcastle upon Tyne NE1 7RU, UK.

\*To whom correspondence should be addressed. E-mail: c.f.barenghi@ncl.ac.uk